Altering the Multimodal Resonance in Ultrathin Silicon Ring for Tunable THz Biosensing

Mohd Salman Khan, Gaurav Varshney, *Member, IEEE*, and Pushpa Giri, *Member, IEEE*

***Abstract*—A technique is implemented for altering the multimodal resonance generated in an ultrathin silicon ring resonator-based terahertz (THz) absorber. The absorber provides the dual-band resonance with the excitation of magnetic and electric dipole in the lower and upper band, respectively. The field of magnetic and electric dipoles is altered using a non-resonant graphene ring placed in the center of the generated dipolar arrangement and the tunability and perfect absorption is achieved. A circuit model is prepared using transmission line method and absorber operation is verified. The proposed absorber can be utilized as a biosensor for the detection of malaria virus and glucose percentage in water. The sensor offers highest sensitivity as 0.29 and 0.27 THz per thickness unit change and quality factor as 117.53 and 245 in the lower and upper band, respectively during the sensing of analyte thickness. Also, it offers the sensitivity as 0.20 and 0.10 THz per refractive index unit change and quality factor as 105.28 and 211.84 in the lower and upper band, respectively during refractive index sensing. Moreover, the structure remains insensitive to polarization angle of the incident electromagnetic wave.**

***Index Terms*—Absorber, bio-sensor, dielectric resonator, dual-band, multimodal resonance, refractive index sensing.**

I. Introduction

THE rich attributes of terahertz (THz) spectrum are enforcing the development of THz systems [1]. The implementation of different THz devices like antennas [2], modulator [3], cloaks [4], absorbers [5], [6] and sensors [7], [8] is on the way. Nowadays, absorbers are being explored for their applications in different domains including medical, defense and communication [9]. The recent development reflects the implementation of ultra-wide [10], wide [11] and narrowband absorbers [12]. Another stream is absorption based biosensing which is being explored [13]–[16]. The biosensing applications require a narrowband absorber [17], [18] with high sensitivity, figure-of merit (FOM), quality factor (Q) and narrow line width defined by full-width-half-maxima (FWHM) [16], [19], [20].

Recently, the artificial material called as metamaterial providing specific range of electrical parameters like permittivity and permeability are being implemented [21], [22]. The metamaterials generally exploit the metal/graphene or dielectrics in the unit cell which provides the resonance [8]. The generated surface plasmons in the metamaterial cells provide the high indexed absorption-based sensing performance [18]. Metals may be good candidate for implementing the THz absorber but their degraded electrical properties restrict the operation of devices at higher frequencies [23]. Also, the metal-based devices are highly sensitive to the temperature variations and environmental effects [7]. The utilization of graphene provides the tunable frequency response which is highly required in the micro/nanoscale devices but it makes the fabrication complex [24], [25]. Another development exploits the dielectric based absorbers [26]. The fabrication of dielectric metamaterial based absorbers in comparison to graphene-based absorbers is realistic in current scenario [27]. Some dielectric-based absorbers have recently been implemented [28]–[33]. The dielectric materials are an efficient choice over others due to their sustainability towards the temperature variations and environmental effects. There are certain limitations also existing with the dielectric based devices which include the large thickness and complex structure [26], [27], [34]. The large thickness may not be compatible with the advancements of the nanoscale systems. Also, the complex structure of dielectric based absorbers becomes a prodigious restriction in the fabrication. Obtaining the broadband absorption spectrum using the dielectric and metal-free absorber is in usual practice [5], [7], [31] but obtaining the narrow band absorption spectrum using the dielectric resonator based absorber is still a challenging task. Also, high sensitivity and Q with other performance parameters is still difficult to achieve in the case of dielectric based absorbers [28]. In fact, obtaining the perfect absorption required for biosensing applications in the case of dielectric based absorber is also a challenging task [33]. Furthermore, the dielectric based absorbers also lack in tunability unlike graphene-based absorbers.

The research issues existing in the literature illustrating the development of dielectric based absorber/biosensors can be summarized in brief as; (i) reducing the thickness so that they can be compatible with the nanoscale systems, (ii) obtaining the efficient performance parameters with desired perfect narrowband absorption so that they can suitably be utilized in the biosensing applications, (iii) simple structure so that fabrication complexity can be mitigated, and (iv) obtaining the tunability in the dielectric based absorbers.

An excellent solution for these issues is reported in this research work. A dielectric metamaterial based dual narrow band, ultrathin, polarization insensitive absorber is

Manuscript received April 14, 2021; revised July 5, 2021; accepted August 14, 2021. Date of publication August 19, 2021; date of current version October 1, 2021. *(Corresponding author: Gaurav Varshney.)*

The authors are with the Department of Electronics and Communication Engineering, National Institute of Technology Patna, Patna 800005, India (e-mail: salmankhanvns@gmail.com; gauravnitd@outlook.com; pushpa.ec@nitp.ac.in).

Digital Object Identifier 10.1109/TNB.2021.3105561

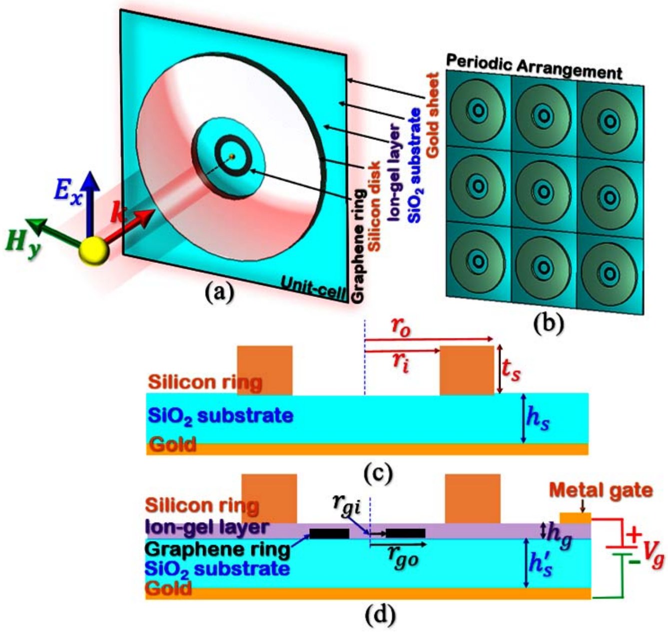

Fig. 1. (a) The unit cell geometry of the proposed absorber, (b) its periodic arrangement, (c) the side-view of the absorber structure without graphene ring and (d) absorber structure with graphene ring and biasing scheme.

implemented with high quality factor and sensitivity. The simple structure of the proposed absorber utilizes an annular silicon ring with overall ultrathin geometry of thickness around $\approx\lambda_o/20$ (λ_o is free space wavelength) which makes it prominent over other dielectric-based absorbers available in literature [28], [31]. In designing, the concept is followed that the magnetic and electric dipoles can separately be excited for obtaining the dual-band resonance in the dielectric based resonator [35]–[37]. The field distribution of electric and magnetic dipoles is altered using a non-resonant graphene ring placed in their center and tunable perfect absorption is achieved. The simple geometry and abundance of silicon material may emphatically mitigate the fabrication complexity which is the main concern of the THz development in current time [36]. The performance of the proposed absorber is also studied for its utilization in the different biosensing applications like detection of virus, glucose in water and as refractive index sensor. The biosensor offers the highest sensitivity as 0.29 and 0.27 THz/thickness unit (TU) and quality factor as 117.53 and 245 in the lower and upper band, respectively during the sensing of analyte thickness. Also, it offers the sensitivity as 0.20 and 0.10 THz/refractive index unit (RIU) and quality factor as 105.28 and 211.84 in the lower and upper band, respectively during refractive index sensing.

II. Design Guidelines

The unit cell structure of silicon-based narrow dual-band absorber is depicted in Fig. 1. A uniform gold layer is grown at one side of the dielectric substrate of silicon dioxide (SiO_2) having relative permittivity $\epsilon_s = 2.25$ with periodicity $p_x = p_y = 85\ \mu m$ along x and $y-$axis, respectively and thickness, $h_s = 0.5\ \mu m$. An annular silicon ring with inner radius, $r_i = 14\ \mu m$, outer radius, $r_o = 35\ \mu m$ and thickness, $t_s = 3.1\ \mu m$ with relative permittivity, $\epsilon_s = 11.9$ is grown at another side of SiO_2 substrate. Here the annular silicon ring is used as the resonating unit of the absorber whose initial dimensions can be selected using procedure given in [27], [34]. The effective outer to inner radius $(r_o - r_i)$ of the proposed absorber is initially taken as of the order of $\approx\lambda_g/2$ with the selection of outer and inner radius as $r_o \approx \lambda_g$ and $r_i \approx \lambda_g/2$, respectively. where, λ_g is the guided wavelength in the high permittivity silicon material at the frequency of fundamental resonance with $\lambda_g = \lambda_o/\sqrt{\epsilon_s}$. The advantage of using metallic plane as reflector is that it offers the characteristics of artificial material in combination with the silicon ring resonator and provides the ultra-thin geometry and thus the overall height of the proposed absorber remains around $\approx \lambda_g/15$. The side view of this structure is shown in Fig. 1(c). This structure provides the resonance with narrow dual-band spectra at a fixed frequency.

The usage of graphene material can offer the tunability and controllability in the frequency response of device by varying its Fermi energy using an external electrostatic bias [38]. Hence, a non-resonant monolayered graphene nano-ring with thickness 0.34 nm and inner and outer radius r_{g_i} and r_{g_o} as 5 and 7 μm, respectively is grown in the centre of the absorber unit cell above the substrate. The electrical properties of the graphene material are selected in accordance to the literature [39], [40]. Initially, the chemical potential of graphene is taken as $\mu_c = 0\ eV$ with the relaxation time $\tau = 0.1\ ps$ at the temperature $T = 300K$ [13]. For achieving the tunability and controllability in the absorber response, the electrostatic biasing can be done on the graphene nano-ring through an ion-gel layer of height $h_g = 0.1\ \mu m$ above the graphene nano-ring [40]. In the case of usage of ion-gel layer, the substrate height is selected as $h'_s = 0.37\ \mu m$ so that the proposed absorber can be utilized as a biosensor in the detection of frequency specific virus/diseases. The utilization of graphene nano-ring causes the generation of surface plasmons on the graphene-air interface and traps the electric charge around its inner and outer periphery. The outer diameter of the graphene nano-ring is selected as $2r_{g_o} \approx \lambda_{sp}/2$. Here, $\frac{\lambda_{sp}}{\lambda_o} \approx \left[\frac{4\alpha}{\epsilon_s+1}\right]\left(\frac{2\pi E_F}{h\omega}\right)$ is the surface plasmons wavelength over the free space wavelength with $\alpha \approx 1/137$ as fine-structure constant, E_F as Fermi energy (0.3 eV) and h is the Plank's constant [41], [42]. This is important to note that graphene nano-ring does not contribute the separate resonance and only affects the level of absorption obtained by the dielectric ring due to the strong confinement of generated graphene surface plasmons. The silicon ring resonator is designed to provide the resonance of electric or magnetic dipole having origin in the centre of the unit cell. Thus, location of graphene nano-ring is selected at the centre of generated dipole i.e. centre of the absorber unit cell so that the field of the generated dipoles can be controlled by the external electrostatic bias applied on graphene. The field distribution on the absorber unit cell is reported in the later section of this manuscript. The dimensions of silicon ring resonator are selected to operate with the fundamental magnetic and electric dipole with the separate resonant frequencies. The placement of graphene ring

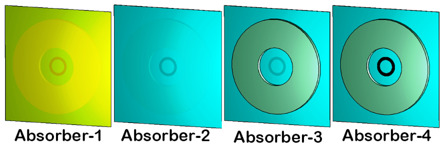

Fig. 2. The evolution of the absorber.

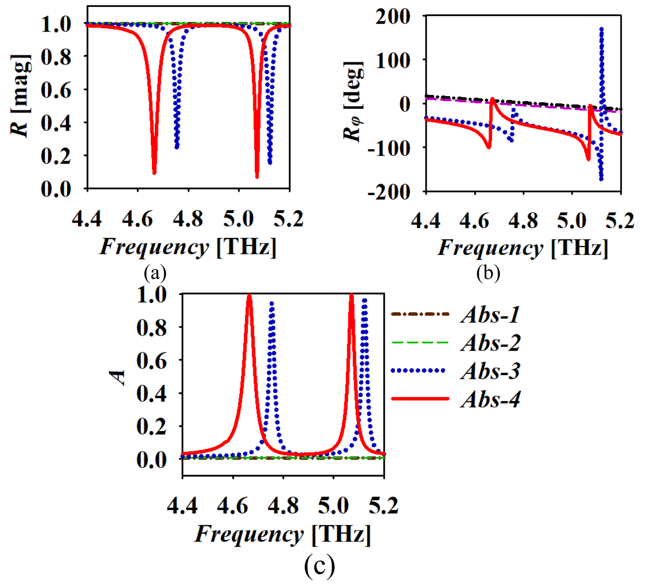

Fig. 3. The frequency response of (a) reflection coefficient, (b) phase of reflection coeffcient and (c) absorption coefficient.

at the centre of the dipole may control its field hence it is placed at the centre with the diameter equivalent to $\lambda_{sp}/2$ at the dominant resonant frequency. Here, $\lambda_{sp} \approx \lambda_o/15$. After calculating the initial values, the final dimensions were obtained by optimizing the structure using CST microwave studio. The floquet ports are used for the unit-cell analysis with the open add space in the direction of propagation and periodicity along the lateral axes. The structure is analysed with the consideration of mesh cell size as $\lambda/15$ with the total number of tetrahedrons of 1,87,987. The thickness of the graphene layer is quite small in comparison to the absorber dimensions hence the mesh cell size is kept small with the adaptive mesh settings [39].

III. Absorber Evolution

The sequential evolution process is analysed for knowing the effect of addition of the different layers used in making the final absorber structure as illustrated in Fig. 2. Fig. 3 shows its frequency response in terms of magnitude and phase of reflection coefficient and magnitude of absorption coefficient. The isolated gold layer provides no absorption and it behaves as a perfect reflector in the operating frequency spectrum with a constant magnitude and phase variation. This is depicted by the structure of absorber-1 in Fig. 2 with the correspoding frequency response in Fig. 3. The coating of gold layer over SiO_2 substrate offering the structure of absorber-2 provides the similar response as absrober-1. The structure of absorber-3 contains a silicon ring grown on another side of the substrate. The frequency plot confirms that resonance dips are obtained due to addition of silicon ring resonator

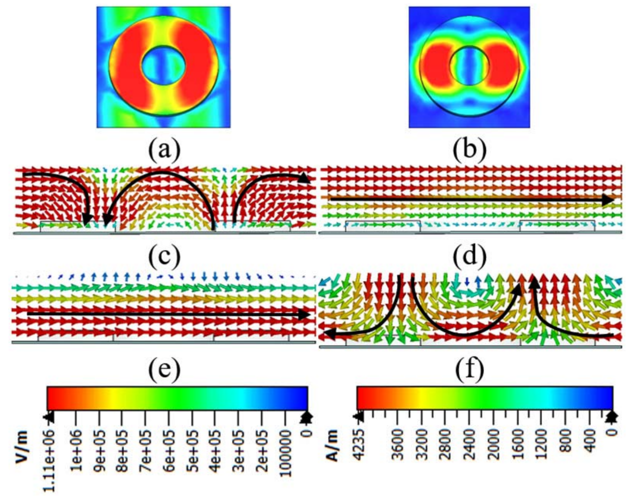

Fig. 4. The electric field distribution in the absorber without graphene ring at frequency (a) 4.75 and (b) 5.12 THz. The electric field vectors (E_x) at frequency (c) 4.75 and (d) 5.12 THz. The magnetic field vectors (H_y) at frequency (e) 4.75 and (f) 5.12 THz (color bar represents the magnitude).

in the absorber structure at frequency 4.75 and 5.12 THz. Correspondingly, there are two phase changes and two absorption peaks in the frequency response. Here, the structure of absorber-3 provides the near perfect absorption with narrow band spectrum and peaks of absorptivity as 0.94 and 0.97 in magnitude at frequencies 4.75 and 5.12 THz, respectively. An annular ring of graphene with thickness 0.34 *nm* is added in the absorber structure with an ion-gel layer coated over it covering the length and width of full substrate. This provides the structrue of absorber-4 which is the final model. The addition of graphene ring shifts the absorption spectrum to the lower side of frequency with the resonant frequency of lower and upper resonance at 4.65 and 5.06 THz, respectively and enhances the level of absorption to more than 99% in both the bands. The phase plot of refelction coefficient confirms two deflections at the corresponding frequencies. As earlier stated that the resonance is obatined from the silicon ring and graphene ring is only used for controlling the obtained resonance, this can also be noticed in the plots. The absorption is evaluated by $A = 1 - T - R$ where A is absorption, $T = |S_{21}|^2$ is transmittance and $R = |S_{11}|^2$ is reflectance. The usage of metallic plane provides the zero transmittance as $T \approx 0$.

IV. Resonant Mode Analysis

The electric and magnetic field distribution is analyzed in the absorber structure for understanding its operation mechanism. Fig. 4 shows the field distribution in the absorber at the resonant frequencies without graphene ring. It follows the fact that both electric and magnetic dipole can be generated in the dielectric based resonator [35]–[37]. The field distribution at the peak absorption frequency of lower band shows the horizontal magnetic field vectors with the encirclement of electric field vectors confirming the generation of a magnetic dipole in the silicon ring resonator. The field distribution at the peak absorption frequency of the upper band shows the linearly distributed horizontal electric field vectors along with

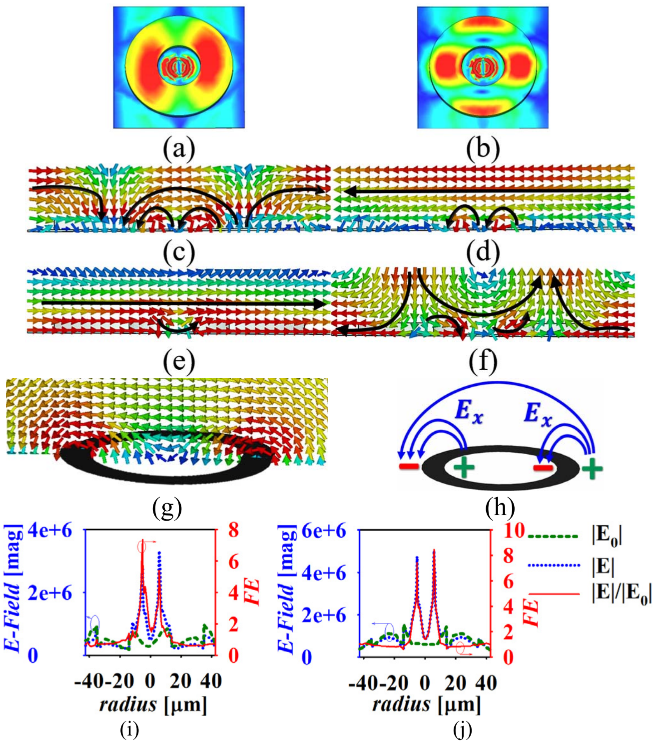

Fig. 5. The electric field distributuion in the absorber with graphene ring at frequency (a) 4.66 and (b) 5.07 THz. The electric field vectors (E_x) at frequency (c) 4.66 and (d) 5.07 THz. The magnetic field vectors (H_y) at frequency (e) 4.66 and (f) 5.07 THz, (g) E_x field distribution showing the created SP due to graphene ring, (h) the electric charge distribution model of graphene ring and the field enhancement in the (i) lower and (j) upper band after placing the graphene ring (color bar is kept similar as in Fig. 4).

the encirclement of the magnetic field lines confirming the generation of an electric dipole. Thus, the absorber without graphene ring operates with multi-modes as the fundamental magnetic dipole in the lower band and fundamental electric dipole in the upper band.

Fig. 5 shows the field distribution in the absorber structure with graphene ring at the peak absorption frequencies. The overall field distribution at the peak frequency of lower band represents the existence of fundamental magnetic dipole with the corresponding loop of electric field. The field distribution at the peak absorption frequency of upper band is drastically affected by the addition of graphene ring and represents the generation of higher order electric dipole. The addition of graphene ring engraves the surface plasmon (SP) mode created on graphene air interface to the electric and magnetic dipole created in the silicon ring as shown in Fig. 5(c) and (d). This results in enhancement in the absorption level. The electric field distribution and its electric charge distribution model around the graphene ring is shown in Fig. 5(g) and 5(h), respectively. Here, the outer diameter of graphene ring is fixed at around $\approx\lambda_{sp}/2$. The increment in outer diameter will shift the overall frequency response to the lower side of frequency scale. Moreover, this is expected that inner diameter of graphene ring will only affect the surface charge accumulated near the inner periphery of graphene ring. Taking the value of inner diameter as zero removes the surface charge accumulated at the inner periphery. Thus, the net charge accumulated at the

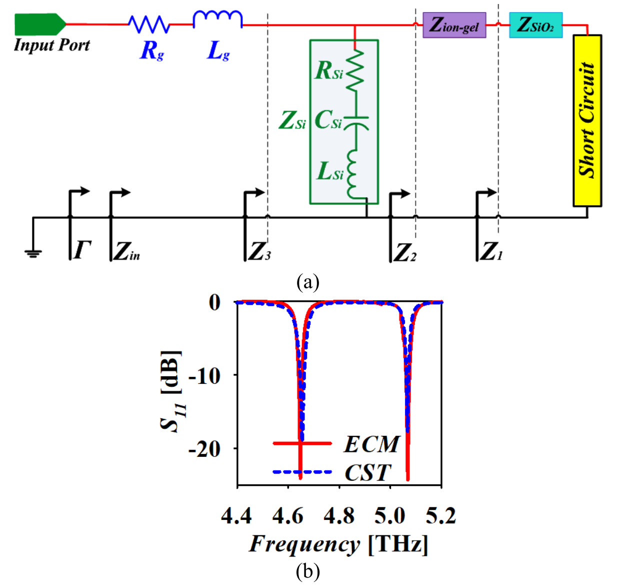

Fig. 6. (a) The electric equivalent circuit model and (b) comparison of the frequency response of S_{11} parameter obtained from the simulation and ECM.

outer periphery only contributes to the total field distribution and hence in the absorber response. This can be verified in SECTION-VI by the parametric variation of r_{g_i} and r_{g_o}. The field distribution is reported for the transverse electric (TE) mode. The field distribution for transverse magnetic (TM) mode can be assumed with the quadrature phase and not reported in this manuscript for brevity.

The field enhancement in the absorber structure after placing the graphene ring is calculated by normalizing the radial electric field component in absorber-4 (with graphene ring), $|E|$ from the radial electric field in absorber-3 (without graphene ring), $|E_0|$. The field enhancement (FE) is calculated by $FE = |E|/|E_0|$ [43], [44]. The magnitude of electric field is taken along the direction where peaks are obtained in Fig. 4(a), (b) and Fig. 5(a), (b) at height $z = 2\ \mu m$. The calculated electric field profile and FE at the resonant frequency of lower and upper band is plotted in Fig. 5(i) and (j), respectively. It can be observed in the plots that field is approximately unaffected in silicon ring after placing the graphene ring. The placement of graphene ring aids in confining the field and thus the peaks of field are obtained on the surface area of the graphene ring. Furthermore, the absorber response remains insensitive to the polarization angle of the incident wave. One limitation of dielectric metamaterial based absorbers is generally noticed i.e. their high sensitivity to the angle of incidence [33]. The dielectric based absorbers allowed the incidence of the electromagnetic wave up to a narrow angle [33]. The frequency response of the proposed absorber is also sensitive to the angle of incidence. Such absorbers are generally suitable for the stationary sensing systems which can be utilized in the applications with the normal incidence.

V. EQUIVALENT CIRCUIT MODELLING AND OPERATION

The operation of the proposed absorber is verified using electrical equivalent circuit model (ECM) prepared using the transmission line method (TLM) as shown in Fig. 6. The

ECM is divided into four sections; first section considers the substrate, second considers the ion-gel, third considers the silicon ring resonator and fourth defines the operation of the graphene ring. The first section having substrate of height h_s placed on the ground plane acts a short-circuited transmission line. This section offers the input impedance as in eq (1).

$$Z_1 = jZ_{SiO_2}\, tan\beta_s h_s \tag{1}$$

Here, $\beta_s = \frac{\omega}{c}\sqrt{\epsilon_s}$ is the propagation constant and $Z_{SiO_2} = Z_o/\sqrt{\epsilon_s}$ is the impedance offered by the substrate with Z_o as free space impedance [40]. The impedance Z_1 acts as the load for second section of the transmission line. The input impedance offered by this section is calculated as in eq (2).

$$Z_2 = Z_{ion-gel}\frac{[Z_1 + jZ_{ion-gel}tan\beta_i h_g]}{[Z_{ion-gel} + jZ_1 tan\beta_i h_g]} \tag{2}$$

Here, $\beta_i = \frac{\omega}{c}\sqrt{\epsilon_{ion-gel}}$ is propagation constant and $Z_{ion-gel} = Z_o/\sqrt{\epsilon_{ion-gel}}$ is the impedance offered by ion-gel layer [40].

The silicon ring resonator offering impedance Z_{Si} placed above the ion-gel layer can be represented by a series RLC resonance circuit for performing the stop band operation. After calculation of the initial electrical parameters of the silicon ring resonator based on the quality factor and the parameter of the transmission line, these were optimized and final values were obtained with the approximate variations [7], [8]. The total input impedance of this circuit is calculated as $Z_3 = Z_{Si}||Z_2$. If input port is applied to the ECM of three sections till silicon ring resonator, this verifies the operation of absorber-3 (Fig. 2). Placing the graphene ring in the structure of absorber-3 shifts its frequency response to the lower side with the improvement in the impedance matching (Fig. 3). Thus, the graphene ring is modelled as the series RL circuit which is applied in the section four of ECM before the input port. The variation in the resistance R_g improves the impedance matching and inductive nature of graphene ring offering inductance L_g shifts the frequency response to the lower side (Fig. 3). The impedance of graphene ring can be calculated as $Z_g = (R_g + j\omega L_g) \approx 1/\sigma_g$. Here, σ_g is the complex surface conductivity of graphene which is calculated based on the Kubo's formalism [45]. The total input impedance of the circuit model is then calculated as $Z_{in} = Z_g + Z_3$. Based on the input impedance, the reflection coefficient is calculated as $\Gamma = \frac{Z_{in}-Z_o}{Z_{in}+Z_o}$ by considering the zero imaginary part at the resonant frequency [46]. Fig. 6(b) shows the simulated frequency response of the proposed absorber in terms of S_{11} parameter illustrating the comparison with the obtained using ECM. The strong agreement in the frequency response confirms the authenticity of the operation of the proposed absorber at the normal incidence. The utilization of ECM for the verification of frequency response is enough because dielectric based absorbers generally remain stable with the normal incidence.

VI. Absorber Performance Analysis

The performance of the proposed absorber is reported with the parametric variations of the physical dimensions as depicted in Fig. 7. In this analysis, the intended single parameter is varied keeping all the other dimensions of the structure constant. Primarily, the emphasis of observation is laid upon the height of the silicon ring resonator, t_s. The operating band of the proposed absorber can be set at different frequencies by varying t_s as shown in Fig. 7(a). The dual-band response can be obtained with $t_s = 3.1\ \mu m$ with the perfect absorption of more than 99%. The further increment in t_s at around its value to 3.7 μm provides another resonance having absorption more than 90%. This shows that variation in t_s can vary the height to radius aspect ratio of the silicon ring resonator which may result in multiple resonance peaks in the absorber response. Other parameters of the silicon ring resonator are r_o and r_i which can change the height to radial distance aspect ratio of the resonator.

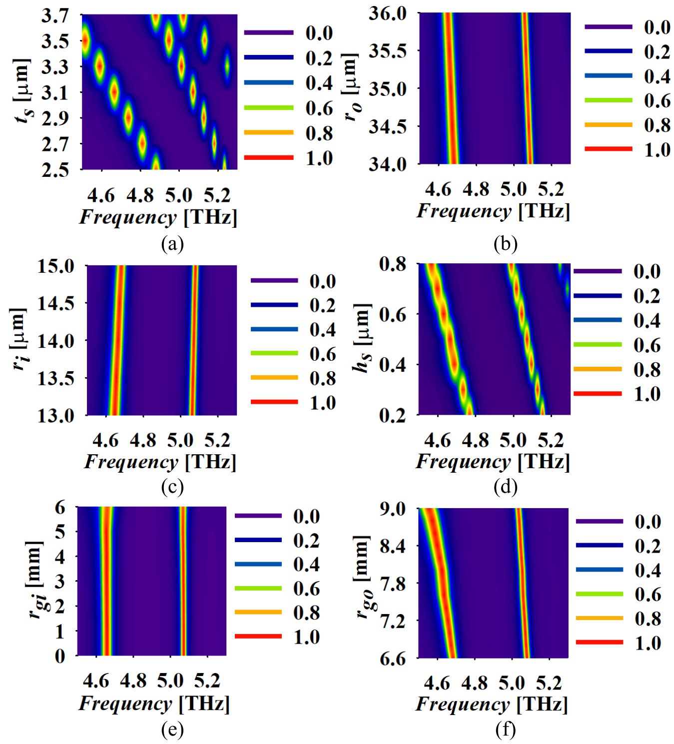

Fig. 7. The absorber performance analysis with the variation in (a) t_s, (b) r_o, (c) r_i (d) h_s, (e) r_{g_i}, and (f) r_{g_o}.

The absorption spectra of the proposed absorber with the variation in these parameters is illustrated in Fig. 7(b) and (c). As expected, the increment in r_o offers the redshift and increment in r_i offers the blueshift in the frequency response following the dielectric waveguide model [47]. Another parameter is thickness of the substrate which affects the frequency response of the absorber drastically as shown in Fig. 7(d). The increment in h_s provides the redshift in the frequency response due to change in the effective height of the absorber unit cell. Fig. 7(e) and (f) shows the frequency response of the proposed absorber with the variation in the inner and outer radius of graphene ring r_{g_i} and r_{g_o}, respectively. The variation in r_{g_i} approximately does not affect the frequency response so it is better to select its value in correlation with μ_c as reported in the next section. The increment in r_{g_o} offers the redshift in the frequency response with high variation in the frequency of

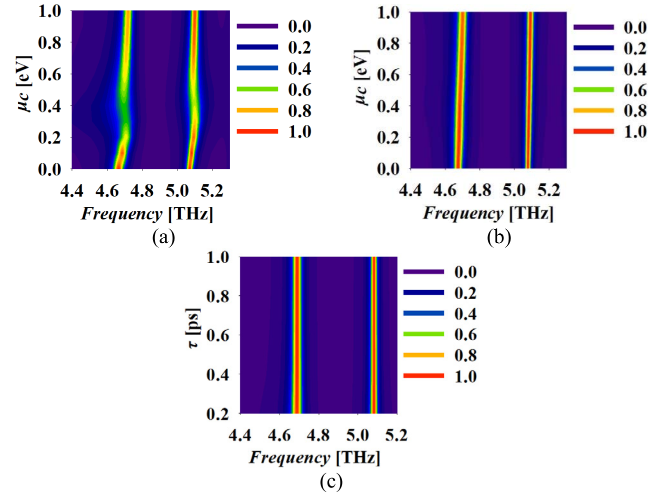

Fig. 8. The absorption spectra with the variation in μ_c with (a) $r_{g_i} = 5\ \mu m$, (b) $r_{g_i} = 0\ \mu m$ taking $\tau = 0.1ps$ and (c) with the variation in τ with $r_{g_i} = 5\ \mu m$ and $\mu_c = 0.1\ eV$.

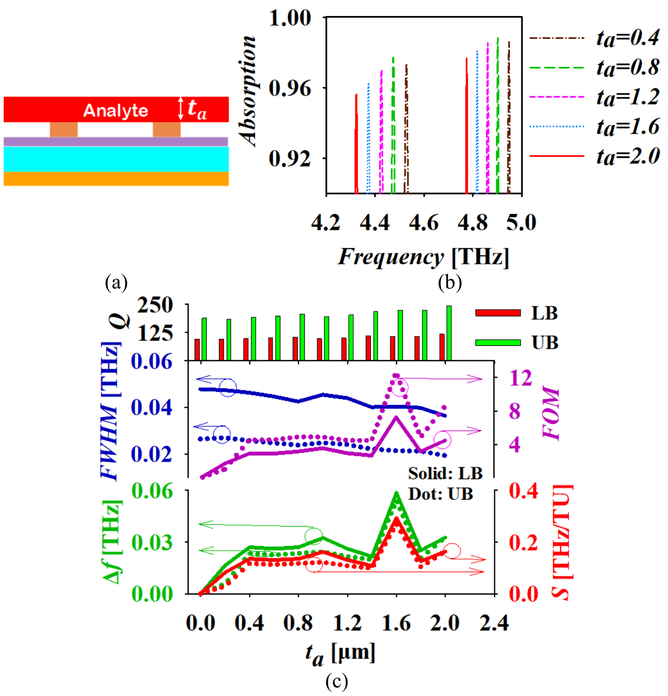

Fig. 9. (a) The absorber structure with the analyte placed at its top, (b) the absorption spectra and (c) different performance parameters with the variation in t_a.

magnetic dipole resonance in the lower band in comparison to the electric dipole in the upper band.

VII. Response Tuning and Controllability

It is stated earlier during the resonant mode analysis reported in Section IV that introduction of graphene ring of diameter of around $\lambda_{sp}/2$ enables the confinement of the electric field. The variation in the conductivity of graphene may allow the changes in the amplitude of the confined field and thus the frequency response of the proposed absorber can be controlled or tuned with the variation in the chemical potential of graphene, μ_c [8], [16]. Here, it is important to note that the resonance obtained from the silicon ring resonator is affected by the variation in the surface conductivity of the graphene ring. Fig. 8(a) represents the effect of variation in μ_c on the absorption spectra. Here, r_{g_i} is selected as $5\ \mu m$. It can be observed in the plot that tunability in the frequency response can be obtained at large scale till $\mu_c \approx 0.2\ eV$. For $0.2 < \mu_c < 0.6\ eV$, the level of absorption is reduced below 50%. For $\mu_c > 0.6\ eV$, the absorption spectrum again attains the value of more than 80% and provides tunable response. Thus, a controllable and tunable response can also be obtained with the different ranges of μ_c with $r_{g_i} = 5\ \mu m$. Fig. 8(b) shows the absorption spectra with the variation in μ_c with $r_{g_i} = 0\ \mu m$. It can be observed that absorption remains more than 80% for all the values of μ_c with this value of r_{g_i}. Thus, r_{g_i} can be selected as $0\ \mu m$ if tunability is the only required aspect without controllability. This may provide ease to fabrication. It is also necessary to understand the effect of quality of graphene on the absorber response by investigating the effect of relaxation time, τ. It is already known that graphene does not participate in the resonance and it only helps in enhancing the impedance matching and providing the tuning in the absorber response hence the variation in τ does not affect it. Fig. 8(c) shows that absorber response is unaffected with the variation in τ.

VIII. Sensing Performance Analysis

A. Analyte Thickness Sensing

The utility of the proposed absorber as a material thickness sensor for varied analyte thickness is investigated with $n = 1.2$. In this investigation pertaining to refractive index sensors, sensitivity (S), figure of merit (FOM), full width at half-maximum (FWHM) and quality Factor (Q) are prominent parameters which demonstrate the extent and quality of sensing trait of the proposed absorber. Fig. 9 shows the absorption spectra and the different performance parameters of the proposed absorber. The sensitivity is calculated as $S = \frac{\Delta f}{\Delta t_a}$ (THz/TU) [17], computes the shift in the frequency of absorption with respect to change in the analyte thickness, Δt_a of the sensing medium under consideration. $\Delta t_a = t_{a2} - t_{a1}$. Here, t_{a_1} and t_{a_2} are the previous and current values of the thickness of the analyte. The absorber provides maximum sensitivity of 0.29 (THz/TU) in the lower band and 0.27 (THz/TU) in the upper band at $t_a = 1.6\,\mu$m. FOM is calculated as $FOM = \frac{S}{FWHM}$. A high FOM of 7.25 in the lower band and 12.64 in the upper band, respectively at $t_a = 1.6\,\mu$m is obtained. FWHM is associated with the ultrathin peak of the sensor proposed in the manuscript. Ultrathin absorption peak demonstrates extremely good selectivity which in turn allows the sensor to detect subtle changes in the material thickness. The absorber offers extremely low values of FWHM. The lowest value of FWHM is 0.0364 THz in the lower band and 0.0193 THz in the upper. Q-factor is calculated as, $Q = \frac{f_p}{FWHM}$. Here, f_p is the peak absorption frequency. The proposed sensor under consideration provides a high Q as 117.53 in the lower band and 245 in the upper band.

B. Refractive Index Sensing

The usage of the proposed absorber is analyzed as the refractive index sensor with $t_a = 0.8\ \mu m$. Fig. 10 shows variation in absorption spectrum over varying refractive index, n for a constant t_a. Here, $S = \frac{\Delta f}{\Delta n}$ (THz/RIU), Δn is

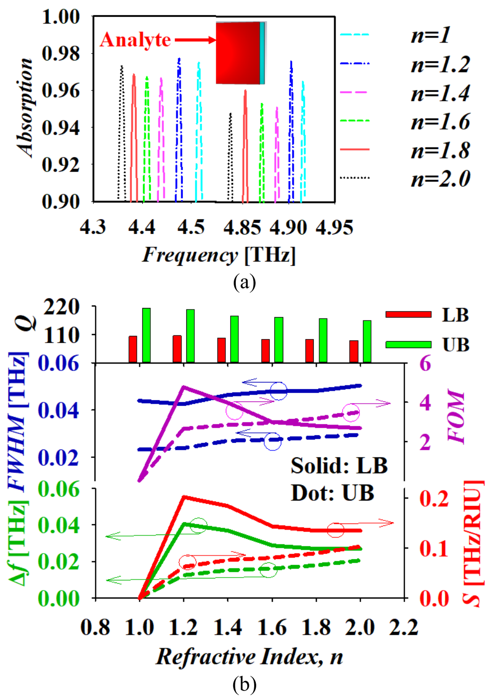

Fig. 10. (a) Absorption spectra and (b) absorber performance analysis with the variation in refractive index of analyte with $t_a = 0.8\ \mu m$.

change in the refractive index of the sensing medium. $\Delta n = n_2 - n_1$ [8], [16]. Here, n_1 and n_2 are the previous and current refractive index of the analyte medium. A maximum sensitivity of 0.20 (THz/RIU) at $n = 1.2$ in lower band and 0.10 (THz/RIU) in upper band at $n = 2$, respectively is obtained. A maximum FOM of 4.76 in the lower band at $n = 1.2$ and 3.50 in the upper band $n = 2$, is observed. Absorber provides the FWHM as 0.0425 and 0.0232 THz in the lower and upper band, respectively. The intended design provides a maximum Q of 105.28 in the lower band and 211.84 in the upper band.

C. Diagnosis of Malaria

The infected RBC in course of malaria infection has refractive index $n_t = 1.383$ and $n_s = 1.373$ in different phases [8], [48]. The sensor under investigation can sense the different phases of malaria disease and performance is reported in TABLE-I with $t_a = 0.8\ \mu m$. The performance of the proposed biosensor is reported in reference to no analyte is placed at its top. The proposed absorber provides a high value of Q-factor with other good sensing parameters.

D. Water/Glucose Detection

The refractive index of water and water with 25% of glucose concentration is $n_w = 1.3198$ and $n_g = 1.3594$, respectively [49]. TABLE-II shows the sensing capability of the proposed sensor in detecting glucose with $t_a = 0.8\ \mu m$. The performance is reported in reference to air as analyte. The performance table shows that the detection of moisture in milieu requiring the pure air like moisture free chambers is also possible with the proposed sensor with efficient performance parameters and high Q-factor.

TABLE I
THE SENSING PERFORMANCE FOR DIAGNOSING MALARIA

Band	n	FWHM (THz)	S (THz/RIU)	FOM (RIU^{-1})	Q
Lower	1.3730	0.0464	0.3600	7.7586	95.7155
	1.3830	0.0464	0.3530	7.6077	95.6961
Upper	1.3730	0.0262	0.2514	9.5954	186.5839
	1.3830	0.0263	0.2472	9.3992	185.8403

TABLE II
SENSING PERFORMANCE FOR GLUCOSE DETECTION

Band	n	FWHM (THz)	S (THz/RIU)	FOM (RIU^{-1})	Q
Lower	1.3198	0.0425	0.3805	8.9529	104.7952
	1.3594	0.0427	0.3536	8.2810	104.1779
Upper	1.3198	0.0242	0.2764	11.4214	202.2272
	1.3594	0.0246	0.2534	10.3048	198.8292

Moreover, the performance of the proposed absorber is tested for the analytes of different materials. The proposed absorber is suitable for the sensing of water ($n = 1.333$), ethanol ($n = 1.36$), ethylene glycol ($n = 1.41$), glycerine ($n = 1.47$), benzene ($n = 1.5$), sodium chloride ($n = 1.54$) and carbon disulphide ($n = 1.63$) with the high sensitivity and other improved performance parameters [50]. Furthermore, the absorber response is also tested for aqueous solutions and polymers having a large value of imaginary part of relative permittivity [51], [52]. The larger value of loss tangent deteriorates the impedance matching and hence the sensing capability of the proposed absorber.

IX. PERFORMANCE COMPARISON

A comparison of the proposed biosensor with the other dual-band absorber/biosensors is reported in TABLE-III. The proposed absorber offers high sensitivity in comparison to many other recently reported refractive index sensors. Also, the proposed sensor provides a significant comparable FOM in comparison to others available in the literature. Also, the absorber offers a significant high Q-factor in comparison to others [20], [53], [54]. Moreover, thickness of the device is another important concern in the implementation of micro/nanoscale systems. The researchers are trying to find the solution for implementing ultrathin geometry. The proposed dual-band absorber/biosensor offers an ultrathin geometry in comparison to others available in the literature. The geometrical symmetricity of the proposed biosensor offers the insensitivity to polarization of the incident angle of the electromagnetic wave which generally remains difficult to obtain in the case of most of dielectric based absorbers [26]. The most important feature with which the modern devices are being implemented is tunability in response. The proposed dielectric based absorber offers the tunability and controllability in its frequency response making it prominent over others.

Since the practical realization of the dielectric-based absorbers and their utilization in the different applications have a significant scope in the near future [36], [55], [56] so it is necessary to report the fabrication steps for the proposed absorber structure. A metal layer can be grown on the SiO_2 substrate at one side using thermal evaporation method. A graphene layer can be prepared on copper foil using chemical vapor deposition method and then transferred on

TABLE III
COMPARISON WITH OTHER BIOSENSORS

Ref	Usage	No. of bands	f (THz)		S (THz/RIU)		FOM $(1/RIU)$		Q		Thickness (μm)	Polarization insensitivity	Tunability
			LB	UB	LB	UB	LB	UB	LB	UB			
[20]	RIS ($t_a = 16\ \mu m$)	Two	1.8	2.26	0.1875	0.360	7.2	19.1	120	94	8.6	Yes	No
[59]	RIS ($t_a = 16\ \mu m$)	Two	1.08	2.77	0.147	0.964	1.21	17.28	8.9	55	10.4	Yes	No
[19]	RIS	Two	1.42	2.99	0.28	1.48	1.2	24.6	7.11	59.8	10.8	Yes	No
[60]	RIS	Two	1.7780	2.4591	-	1.90	-	229	6.91	296	4.8	No	No
[61]	RIS	Two	0.76	1.28	0.47	0.51	9.4	14.4	23	3.7	5.4	Yes	No
[62]	TS ($n = 1.6$)	Single	0.6	-	0.007	-	2.3	-	11.6	-	518.2	Yes	No
	TS ($n = 1.6$)		0.75	-	0.00618	-	1.98	-	11	-			
[17]	RIS ($t_a = 1\ \mu m$)	Single	2.249	-	0.3	-	2.94	-	22.05	-	10.4	No	No
	TS ($n = 1.35$)		2.145	-	0.0237*	-	0.23	-	20.43	-			
This work	RIS ($t_a = 0.8\ \mu m$)	Two	4.515	4.9146	0.20	0.10	4.76	3.50	105.28	211.84	3.65	Yes	Yes
	TS ($n = 1.2$)		4.5546	4.9713	0.29*	0.27*	7.25	12.64	117.53	245			

LB-lower band, UB- upper band, RIS-performance as refractive index sensor and TS-performance as thickness sensor, *sensitivity in $THz/\mu m$

another side of the SiO_2 substrate [57], [58]. The transferred graphene sheet can be patterned to form a graphene ring. An ion-gel layer can then be deposited above the structure of graphene ring placed above the substrate using thermal evaporation method [40]. The silicon ring can be fabricated on the ion-gel layer using photolithography based on the large-scale microfabrication techniques [56]. Also, a metal gate can be grown on the edge of the absorber unit cell for connecting the bias voltage.

X. CONCLUSION

A technique has been implemented for altering the multimodal resonance generated in an ultrathin silicon ring resonator-based THz absorber. The dual-band resonance with the excitation of magnetic and electric dipole in the lower and upper band, respectively has been obtained. The field distribution of magnetic and electric dipoles has been altered using a non-resonant graphene ring placed in the center of the generated dipolar arrangement in the silicon ring and thus the tunability and perfect absorption is achieved. The absorber operation has been verified by the response obtained from the circuit model made by using transmission line method. Moreover, the proposed absorber has been proved as an efficient THz biosensor and analyzed for the sensing of different viruses, water and water with glucose. The performance of the proposed absorber is analyzed as a biosensor for the sensing of malaria virus and percentage of glucose in water. The biosensor offers highest sensitivity as 0.29 and 0.27 THz/TU and quality factor as 117.53 and 245 in the lower and upper band, respectively during the sensing of analyte thickness. Also, it offers the sensitivity as 0.20 and 0.10 THz/RIU and quality factor as 105.28 and 211.84 in the lower and upper band, respectively during refractive index sensing. Moreover, absorber provides the response insensitive to polarization angle.

REFERENCES

[1] I. F. Akyildiz, J. M. Jornet, and C. Han, "Terahertz band: Next frontier for wireless communications," *Phys. Commun.*, vol. 12, pp. 16–32, Sep. 2014, doi: 10.1016/j.phycom.2014.01.006.

[2] G. Varshney, "Reconfigurable graphene antenna for THz applications: A mode conversion approach," *Nanotechnology*, vol. 31, no. 13, Mar. 2020, Art. no. 135208, doi: 10.1088/1361-6528/ab60cc.

[3] S. Savo, D. Shrekenhamer, and W. J. Padilla, "Liquid crystal metamaterial absorber spatial light modulator for THz applications," *Adv. Opt. Mater.*, vol. 2, no. 3, pp. 275–279, Mar. 2014, doi: 10.1002/adom.201300384.

[4] P.-Y. Chen and A. Alù, "Atomically thin surface cloak using graphene monolayers," *ACS Nano*, vol. 5, no. 7, pp. 5855–5863, 2011, doi: 10.1021/nn201622e.

[5] G. Varshney, N. Rani, V. S. Pandey, R. S. Yaduvanshi, and D. Singh, "Graphite/graphene disk stack-based metal-free wideband terahertz absorber," *J. Opt. Soc. Amer. B, Opt. Phys.*, vol. 38, no. 1, pp. 1–9, 2021.

[6] A. K. Soni and G. Varshney, "Multiband generation and absorption enhancement in a graphite-based metal-free absorber," *Plasmonics*, vol. 16, no. 1, pp. 241–252, Feb. 2021, doi: 10.1007/s11468-020-01286-5.

[7] G. Varshney, "Wideband THz absorber: By merging the resonance of dielectric cavity and graphite disk resonator," *IEEE Sensors J.*, vol. 21, no. 2, pp. 1635–1643, Jan. 2021, doi: 10.1109/JSEN.2020.3017454.

[8] M. Nejat and N. Nozhat, "Ultrasensitive THz refractive index sensor based on a controllable perfect MTM absorber," *IEEE Sensors J.*, vol. 19, no. 22, pp. 10490–10497, Nov. 2019, doi: 10.1109/JSEN.2019.2931057.

[9] A. Y. Pawar, D. D. Sonawane, K. B. Erande, and D. V. Derle, "Terahertz technology and its applications," *Drug Invention Today*, vol. 5, no. 2, pp. 157–163, 2013, doi: 10.1016/j.dit.2013.03.009.

[10] M. Aalizadeh, A. Khavasi, B. Butun, and E. Ozbay, "Large-area, cost-effective, ultra-broadband perfect absorber utilizing manganese in metal-insulator-metal structure," *Sci. Rep.*, vol. 8, no. 1, pp. 1–13, Dec. 2018, doi: 10.1038/s41598-018-27397-y.

[11] C. Gong *et al.*, "Broadband terahertz metamaterial absorber based on sectional asymmetric structures," *Sci. Rep.*, vol. 6, no. 1, pp. 1–8, Oct. 2016, doi: 10.1038/srep32466.

[12] B.-X. Wang, W.-Q. Huang, and L.-L. Wang, "Ultra-narrow terahertz perfect light absorber based on surface lattice resonance of a sandwich resonator for sensing applications," *RSC Adv.*, vol. 7, no. 68, pp. 42956–42963, 2017, doi: 10.1039/c7ra08413g.

[13] S. Asgari, N. Granpayeh, and T. Fabritius, "Controllable terahertz cross-shaped three-dimensional graphene intrinsically chiral metastructure and its biosensing application," *Opt. Commun.*, vol. 474, Nov. 2020, Art. no. 126080, doi: 10.1016/j.optcom.2020.126080.

[14] A. Ahmadivand, B. Gerislioglu, Z. Ramezani, A. Kaushik, P. Manickam, and S. A. Ghoreishi, "Functionalized terahertz plasmonic metasensors: Femtomolar-level detection of SARS-CoV-2 spike proteins," *Biosens. Bioelectron.*, vol. 177, pp. 1–21, Apr. 2021, doi: 10.1016/j.bios.2021.112971.

[15] A. Ahmadivand, B. Gerislioglu, R. Ahuja, and Y. Kumar Mishra, "Terahertz plasmonics: The rise of toroidal metadevices towards immunobiosensings," *Mater. Today*, vol. 32, pp. 108–130, Jan. 2020, doi: 10.1016/j.mattod.2019.08.002.

[16] F. Yan *et al.*, "Ultrasensitive tunable terahertz sensor with graphene plasmonic grating," *J. Lightw. Technol.*, vol. 37, no. 4, pp. 1103–1112, 2019, doi: 10.1109/JLT.2018.2886412.

[17] A. S. Saadeldin, M. F. O. Hameed, E. M. A. Elkaramany, and S. S. A. Obayya, "Highly sensitive terahertz metamaterial sensor," *IEEE Sensors J.*, vol. 19, no. 18, pp. 7993–7999, Sep. 2019, doi: 10.1109/JSEN.2019.2918214.

[18] Z. Vafapour, "Polarization-independent perfect optical metamaterial absorber as a glucose sensor in food industry applications," *IEEE Trans. Nanobiosci.*, vol. 18, no. 4, pp. 622–627, Oct. 2019, doi: 10.1109/TNB.2019.2929802.

[19] B.-X. Wang, X. Zhai, G.-Z. Wang, W.-Q. Huang, and L.-L. Wang, "A novel dual-band terahertz metamaterial absorber for a sensor application," *J. Appl. Phys.*, vol. 117, no. 1, Jan. 2015, Art. no. 014504, doi: 10.1063/1.4905261.

[20] M. Janneh, A. De Marcellis, E. Palange, A. T. Tenggara, and D. Byun, "Design of a metasurface-based dual-band terahertz perfect absorber with very high Q-factors for sensing applications," *Opt. Commun.*, vol. 416, pp. 152–159, Jun. 2018, doi: 10.1016/j.optcom.2018.02.013.

[21] H.-T. Chen, "Interference theory of metamaterial perfect absorbers," *Opt. Exp.*, vol. 20, no. 7, p. 7165, Mar. 2012, doi: 10.1364/oe.20.007165.

[22] X. Shen *et al.*, "Triple-band terahertz metamaterial absorber: Design, experiment, and physical interpretation," *Appl. Phys. Lett.*, vol. 101, no. 15, Oct. 2012, Art. no. 154102, doi: 10.1063/1.4757879.

[23] M. Walther, D. G. Cooke, C. Sherstan, M. Hajar, M. R. Freeman, and F. A. Hegmann, "Terahertz conductivity of thin gold films at the metal-insulator percolation transition," *Phys. Rev. B, Condens. Matter*, vol. 76, no. 12, pp. 1–9, Sep. 2007, doi: 10.1103/PhysRevB.76.125408.

[24] X.-D. Chen *et al.*, "High-quality and efficient transfer of large-area graphene films onto different substrates," *Carbon*, vol. 56, pp. 271–278, May 2013, doi: 10.1016/j.carbon.2013.01.011.

[25] P. Xiang *et al.*, "*In situ* synthesis of monolayer graphene on silicon for near-infrared photodetectors," *RSC Adv.*, vol. 9, no. 64, pp. 37512–37517, Nov. 2019, doi: 10.1039/c9ra06792b.

[26] Y.-L. Liao and Y. Zhao, "Ultra-narrowband dielectric metamaterial absorber with ultra-sparse nanowire grids for sensing applications," *Sci. Rep.*, vol. 10, no. 1, pp. 1–7, Dec. 2020, doi: 10.1038/s41598-020-58456-y.

[27] X. Liu, K. Fan, I. V. Shadrivov, and W. J. Padilla, "Experimental realization of a terahertz all-dielectric metasurface absorber," *Opt. Exp.*, vol. 25, no. 1, p. 191, Jan. 2017, doi: 10.1364/oe.25.000191.

[28] P. Nie, D. Zhu, Z. Cui, F. Qu, L. Lin, and Y. Wang, "Sensitive detection of chlorpyrifos pesticide using an all-dielectric broadband terahertz metamaterial absorber," *Sens. Actuators B, Chem.*, vol. 307, Mar. 2020, Art. no. 127642, doi: 10.1016/j.snb.2019.127642.

[29] J. Zi *et al.*, "Terahertz polarization converter based on all-dielectric high birefringence metamaterial with elliptical air holes," *Opt. Commun.*, vol. 416, pp. 130–136, Jun. 2018, doi: 10.1016/j.optcom.2018.02.012.

[30] W. Su, Z. Geng, J. Qi, and H. Wu, "Multi-fano resonances in graphene coated all-dielectric metasurface for refractive index sensing with high figure of merits," *IEEE J. Sel. Topics Quantum Electron.*, vol. 27, no. 1, pp. 1–6, Jan. 2021, doi: 10.1109/JSTQE.2020.2991884.

[31] J. Wang, T. Lang, T. Shen, C. Shen, Z. Hong, and C. Lu, "Numerical study of an ultra-broadband all-silicon terahertz absorber," *Appl. Sci.*, vol. 10, no. 2, p. 436, Jan. 2020.

[32] P. Moitra, B. A. Slovick, Z. Gang Yu, S. Krishnamurthy, and J. Valentine, "Experimental demonstration of a broadband all-dielectric metamaterial perfect reflector," *Appl. Phys. Lett.*, vol. 104, no. 17, Apr. 2014, Art. no. 171102, doi: 10.1063/1.4873521.

[33] J. Zhou, S. Yan, C. Li, J. Zhu, and Q. H. Liu, "Perfect ultraviolet absorption in graphene using the magnetic resonance of an all-dielectric nanostructure," *Opt. Exp.*, vol. 26, no. 14, Jul. 2018, Art. no. 18155, doi: 10.1364/oe.26.018155.

[34] K. Fan, J. Y. Suen, X. Liu, and W. J. Padilla, "All-dielectric metasurface absorbers for uncooled terahertz imaging," *Optica*, vol. 4, no. 6, p. 601, Jun. 2017, doi: 10.1364/optica.4.000601.

[35] M. A. Abbas *et al.*, "Engineering multimodal dielectric resonance of TiO_2 based nanostructures for high-performance refractive index sensing applications," *Opt. Exp.*, vol. 28, no. 16, Aug. 2020, Art. no. 23509, doi: 10.1364/oe.397431.

[36] A. J. Ollanik, I. O. Oguntoye, G. Z. Hartfield, and M. D. Escarra, "Highly sensitive, affordable, and adaptable refractive index sensing with silicon-based dielectric metasurfaces," *Adv. Mater. Technol.*, vol. 4, no. 2, pp. 1–9, 2019, doi: 10.1002/admt.201800567.

[37] Y. Zhang *et al.*, "High-quality-factor multiple Fano resonances for refractive index sensing," *Opt. Lett.*, vol. 43, no. 8, p. 1842, Apr. 2018, doi: 10.1364/ol.43.001842.

[38] A. Vakil and N. Engheta, "Transformation optics using graphene," *Science*, vol. 332, no. 6035, pp. 1291–1294, 2011, doi: 10.1126/science.1202691.

[39] P. Kumar, A. Lakhtakia, and P. K. Jain, "Graphene pixel-based polarization-insensitive metasurface for almost perfect and wideband terahertz absorption," *J. Opt. Soc. Amer. B, Opt. Phys.*, vol. 36, no. 8, p. F84, Aug. 2019, doi: 10.1364/josab.36.000f84.

[40] S. Asgari and T. Fabritius, "Equivalent circuit model of graphene chiral multi-band metadevice absorber composed of U-shaped resonator array," *Opt. Exp.*, vol. 28, no. 26, Dec. 2020, Art. no. 39850, doi: 10.1364/oe.412107.

[41] F. H. L. Koppens, D. E. Chang, and F. J. G. de Abajo, "Graphene plasmonics: A platform for strong light–matter interactions," *Nano Lett.*, vol. 11, no. 8, pp. 3370–3377, Aug. 2011.

[42] F. H. L. MinovKoppensich, D. E. Chang, S. Thongrattanasiri, and F. J. G. G. de Abajo, "Graphene plasmonics: A platform for strong light–matter interactions," *Opt. Photon. News*, vol. 22, no. 12, p. 36, Dec. 2011, doi: 10.1364/opn.22.12.000036.

[43] M. Darvishzadeh-Varcheie, C. Guclu, R. Ragan, O. Boyraz, and F. Capolino, "Electric field enhancement with plasmonic colloidal nanoantennas excited by a silicon nitride waveguide," *Opt. Exp.*, vol. 24, no. 25, Dec. 2016, Art. no. 28337, doi: 10.1364/oe.24.028337.

[44] A. Forouzmand, H. M. Bernety, and A. B. Yakovlev, "Graphene-loaded wire medium for tunable broadband subwavelength imaging," *Phys. Rev. B, Condens. Matter*, vol. 92, no. 8, pp. 1–14, Aug. 2015, doi: 10.1103/PhysRevB.92.085402.

[45] R. Mishra, R. Panwar, and D. Singh, "An efficient equivalent circuit modelling approach for optimal design of frequency selective surface and graphene integrated THz metamaterial absorber," *IEEE Magn. Lett.*, vol. 9, pp. 1–5, 2018, doi: 10.1109/LMAG.2018.2878946.

[46] M. S. Islam, J. Sultana, M. Biabanifard, Z. Vafapour, M. J. Nine, and A. Dinovitser, "Tunable localized surface plasmon graphene metasurface for multiband superabsorption and terahertz sensing," *Carbon*, vol. 158, pp. 559–567, Mar. 2020, doi: 10.1016/j.carbon.2019.11.026.

[47] E. A. J. Marcatili, "Dielectric rectangular waveguide and directional coupler for integrated optics," *Bell Syst. Tech. J.*, vol. 48, no. 7, pp. 2071–2102, Sep. 1969, doi: 10.1002/j.1538-7305.1969.tb01166.x.

[48] P. Y. Liu *et al.*, "Cell refractive index for cell biology and disease diagnosis: Past, present and future," *Lab. Chip*, vol. 16, no. 4, pp. 634–644, Dec. 2016, doi: 10.1039/c5lc01445j.

[49] G. Li *et al.*, "A novel plasmonic resonance sensor based on an infrared perfect absorber," *J. Phys. D, Appl. Phys.*, vol. 45, no. 20, May 2012, Art. no. 205102, doi: 10.1088/0022-3727/45/20/205102.

[50] R. Ke, W. Liu, J. Tian, R. Yang, and W. Pei, "Dual-band tunable perfect absorber based on monolayer graphene pattern," *Results Phys.*, vol. 18, Sep. 2020, Art. no. 103306, doi: 10.1016/j.rinp.2020.103306.

[51] Y. Hasegawa, Y. Ohki, K. Fukunaga, M. Mizuno, and K. Sasaki, "Complex permittivity spectra of various insulating polymers at ultrawide-band frequencies," *Electr. Eng. Jpn.*, vol. 198, no. 3, pp. 11–18, Feb. 2017, doi: 10.1002/eej.22925.

[52] A. De Ninno, E. Nikollari, M. Missori, and F. Frezza, "Dielectric permittivity of aqueous solutions of electrolytes probed by THz time-domain and FTIR spectroscopy," *Phys. Lett. A*, vol. 384, no. 34, Dec. 2020, Art. no. 126865, doi: 10.1016/j.physleta.2020.126865.

[53] R. Singh, W. Cao, I. Al-Naib, L. Cong, W. Withayachumnankul, and W. Zhang, "Ultrasensitive terahertz sensing with high-Q Fano resonances in metasurfaces," *Appl. Phys. Lett.*, vol. 105, no. 17, Oct. 2014, Art. no. 171101, doi: 10.1063/1.4895595.

[54] T. Chen, R. Zhao, and B. X. Wang, "Theoretical investigation of a simple design of triple-band terahertz metamaterial absorber for high-Q sensing," *Appl. Sci.*, vol. 9, no. 7, pp. 31–33, 2019, doi: 10.3390/app9071410.

[55] K. Gorgulu, A. Gok, M. Yilmaz, K. Topalli, N. Bıyıklı, and A. K. Okyay, "All-silicon ultra-broadband infrared light absorbers," *Sci. Rep.*, vol. 6, no. 1, pp. 1–7, Dec. 2016, doi: 10.1038/srep38589.

[56] Y. Wang *et al.*, "All-dielectric terahertz plasmonic metamaterial absorbers and high-sensitivity sensing," *ACS Omega*, vol. 4, no. 20, pp. 18645–18652, Nov. 2019, doi: 10.1021/acsomega.9b02506.

[57] H. Hu *et al.*, "Broadly tunable graphene plasmons using an ion-gel top gate with low control voltage," *Nanoscale*, vol. 7, no. 46, pp. 19493–19500, 2015, doi: 10.1039/c5nr05175d.

[58] V. Thareja *et al.*, "Electrically tunable coherent optical absorption in graphene with ion gel," *Nano Lett.*, vol. 15, no. 3, pp. 1570–1576, 2015, doi: 10.1021/nl503431d.

[59] X. Yan, L.-J. Liang, X. Ding, and J.-Q. Yao, "Solid analyte and aqueous solutions sensing based on a flexible terahertz dual-band metamaterial absorber," *Opt. Eng.*, vol. 56, no. 2, Feb. 2017, Art. no. 027104, doi: 10.1117/1.oe.56.2.027104.

[60] B.-X. Wang, Y. He, P. Lou, and W. Xing, "Design of a dual-band terahertz metamaterial absorber using two identical square patches for sensing application," *Nanosc. Adv.*, vol. 2, no. 2, pp. 763–769, Feb. 2020, doi: 10.1039/c9na00770a.

[61] F. Lan *et al.*, "Dual-band refractometric terahertz biosensing with intense wave-matter-overlap microfluidic channel," *Biomed. Opt. Exp.*, vol. 10, no. 8, p. 3789, Aug. 2019, doi: 10.1364/boe.10.003789.

[62] L. Cong, S. Tan, R. Yahiaoui, F. Yan, W. Zhang, and R. Singh, "Experimental demonstration of ultrasensitive sensing with terahertz metamaterial absorbers: A comparison with the metasurfaces," *Appl. Phys. Lett.*, vol. 106, no. 3, Jan. 2015, Art. no. 031107, doi: 10.1063/1.4906109.